Journal of Magnetism and Magnetic Materials 622 (2025) 172963

Contents lists available at ScienceDirect

Journal of Magnetism and Magnetic Materials

journal homepage: www.elsevier.com/locate/jmmm

Research article

Magnetic structure and magnetodielectric behavior of the chiral magnet $CoTeMoO_6$

Brady Wilson [a], Ananta Raj Acharya [b], Eun Sang Choi [c], Ram Rai [d], Qiang Zhang [e], Stuart Calder [e], Rafael Gonzalez-Hernandez [f], Jonathan Guerrero Sanchez [g], Chetan Dhital [a,*]

[a] Department of Physics, Kennesaw State University, Marietta, GA, USA
[b] Georgia State University, Perimeter College, Alpharetta, GA, USA
[c] National High Magnetic Field Laboratory, Tallahassee, FL, USA
[d] Department of Physics, SUNY Buffalo State, Buffalo, NY, USA
[e] Neutron Scattering Division, Oak Ridge National Laboratory, Oak Ridge, TN, USA
[f] Departamento de Física y Geociencias, Universidad del Norte, Barranquilla, Colombia
[g] Centro de Nanociencias y Nanotecnología, Universidad Nacional Autónoma de México, Ensenada, BC, Mexico

ARTICLE INFO

Keywords:
Magnetic structure
Magnetodielectric coupling
Canted magnetism
Chiral magnet
Spin-phonon coupling

ABSTRACT

We investigate the magnetic structure and magnetodielectric behavior of the chiral magnet $CoTeMoO_6$ (CTMO) through neutron diffraction, magnetization, and magnetodielectric measurements, complemented by density functional theory (DFT) calculations. Our findings reveal a canted magnetic structure with moments confined to the *ab* plane, giving rise to weak ferromagnetism under an external magnetic field. Additionally, we observe magnetodielectric coupling that strongly correlates with the magnetic ordering temperature and magnetic structure. These results are discussed in the context of potential mechanisms involving spin-dependent *p-d* hybridization and spin-phonon coupling.

1. Introduction

Insulating magnetic oxides have attracted considerable scientific interest due to their diverse emergent phenomena and multifunctional properties, which result from the intricate interplay among spin, charge, lattice, and orbital degrees of freedom [1–4]. These materials provide an ideal platform for exploring fundamental physics and advancing applications in spintronics, magnetoelectrics, and energy-efficient technologies [2,5,6].

Despite the significant disparity in energy scales between electronic band gaps (typically in the range of eV) and magnetic interactions (on the order of meV), magnetic insulators frequently exhibit strong coupling between their electrical and magnetic properties [7,8]. This coupling, commonly referred to as *magnetoelectric coupling*, manifests in two primary forms: (i) magnetoelectric multiferroics, characterized by spontaneous macroscopic polarization coupled to magnetism, and (ii) magnetodielectrics, which exhibit coupling between magnetism and dielectric constant but may or may not exhibit spontaneous polarization. While all magnetoelectric multiferroics are inherently magnetodielectric, the reverse does not necessarily hold.

The underlying mechanisms driving magnetoelectric and magnetodielectric phenomena are often attributed to spin driven phenomena, whereby magnetic order influences dielectric properties through pathways such as spin-phonon coupling, exchange-striction, inverse Dzyaloshinskii–Moriya interactions, or metal-ligand hybridization processes [4,9–11]. Transition metal and rare-earth oxides frequently exhibit these phenomena, accompanied by anomalies in dielectric constants, magnetocapacitance, and other physical properties near magnetic ordering temperatures or during field-induced magnetic transitions [7,8,12–30]. Unlike magnetoelectric multiferroics, which require specific symmetry constraints, magnetodielectric effects occur in a broader range of materials, including both polar and non-polar structures [13–15,19,20,22]. Oxides crystallizing in chiral or polar space groups are particularly appealing, as they often host unconventional magnetic structures such as helimagnets, skyrmions, or canted antiferromagnetic phases. These materials exhibit strongly coupled magnetic and dipolar properties, which can be tuned using external electric and magnetic fields. Notable examples include Cu_2OSeO_3 [31–33] a prominent skyrmion-hosting multiferroic, and polar compounds such as $Ba_2MGe_2O_7$ (M=Co, Cu, Mn), which display pronounced spin-driven magnetoelectric effects [34–36].

In this study, we focus on the chiral magnet $CoTeMoO_6$ (CTMO), leveraging an integrative approach combining comprehensive experimental and theoretical investigations. CTMO crystallizes in a chiral

* Corresponding author.
E-mail address: cdhital@kennesaw.edu (C. Dhital).

https://doi.org/10.1016/j.jmmm.2025.172963
Received 27 January 2025; Received in revised form 7 March 2025; Accepted 12 March 2025
Available online 21 March 2025

orthorhombic structure (space group $P2_12_12$) with lattice parameters $a = 5.2406(2)$ Å, $b = 5.0543(2)$ Å, and $c = 8.8156(3)$ Å. The CoO_6 octahedra form corner-sharing networks within the ab plane, creating chiral chains of Co ions along the [100] and [010] directions. At $T = 2$ K, the atomic positions in CTMO are as follows: Co^{2+} on site 2a $(0, 0, 0.5239(2))$, Te^{4+} on site 2b $(0, 0.5, 0.254(9))$, Mo^{6+} on site 2b $(0, 0.5, 0.809(8))$, O1 on site 4c $(0.296(11), 0.847(11), 0.073(6))$, O2 on site 4c $(0.185(12), 0.761(15), 0.702(6))$, and O3 on site 4c $(0.179(13), 0.720(10), 0.392(5))$. The intrinsic chirality of $CoTeMoO_6$, combined with the magnetic and electronic properties of Co^{2+} ions, further enhances its potential for complex magnetic interactions, including Dzyaloshinskii–Moriya (DM) interactions and anisotropic exchange coupling. These structural features and magnetic interactions make CTMO a compelling candidate for studying spin-driven magnetodielectric effects.

Previous studies on CTMO have identified a canted antiferromagnetic structure at zero magnetic field, accompanied by significant magnetocapacitance anomalies near the magnetic transition temperature [37–39]. While those previous studies suggest spin-phonon coupling as a possible mechanism, definitive evidence remains elusive. Moreover, the connections between spin fluctuations near the ordering temperature, field-induced magnetic transitions, and magnetodielectric effects are not fully understood. The evolution of the magnetic structure under applied magnetic fields has similarly not been comprehensively explored.

To address these gaps, we investigate the magnetodielectric and magnetic properties of polycrystalline CTMO. Through DC and AC susceptibility, magnetization, and magnetocapacitance measurements, we delve into the spin dynamics and magnetodielectric coupling in CTMO. Neutron diffraction studies, conducted at zero field and under a 50 kOe magnetic field, provide detailed insights into the evolution of the magnetic structure, highlighting the roles of DM interactions and spin anisotropies. The obtained magnetic structures are further substantiated by density functional theory (DFT) calculations indicating the validity of the obtained magnetic structures.

We also compare CTMO with its isostructural counterpart $MnTeMoO_6$ (MTMO), which, despite its structural similarity, does not exhibit magnetodielectric effects. This comparative analysis underscores the critical role of Co^{2+} ions and their associated spin–orbit and orbital-lattice interactions in driving the observed phenomena in CTMO. Finally, our findings are contextualized within the broader landscape of spin-driven mechanisms, including p-d exchange interactions and spin-phonon coupling, drawing parallels with other chiral magnets such as Cu_2OSeO_3 and polar magnet $Ba_2MGe_2O_7$.

Our results position CTMO as a model system for the study of intrinsic spin-driven magnetodielectric coupling, offering a robust platform for future investigations into the intricate interplay between magnetism and dielectric properties in chiral magnetic oxides.

2. Experimental methods

2.1. Synthesis

Polycrystalline samples of (CTMO) and (MTMO) were synthesized using a solid-state reaction method suggested in previous studies [37–39]. Stoichiometric amounts of high-purity CoO, TeO_2, and MoO_3 were mixed for CTMO, while MnO was substituted for CoO in the synthesis of MTMO. The mixtures were sealed in quartz tubes to prevent oxidation and annealed at temperatures of 540 °C to 550 °C for CTMO and 550 °C to 580 °C for MTMO, with multiple intermediate grinding steps to ensure homogeneity. Phase purity and crystallinity of the samples were verified using X-ray diffraction measurements.

2.2. Magnetization measurements

DC and AC magnetization measurements were performed using a superconducting quantum interference device (SQUID) magnetometer at the National High Magnetic Field Laboratory and a vibrating sample magnetometer at SUNY Buffalo State. Zero-field-cooled (ZFC) and field-cooled (FC) protocols were employed to investigate magnetic ordering. AC susceptibility measurements were also conducted to probe low frequency spin dynamics during magnetic transitions.

2.3. Dielectric and magnetocapacitance measurements

The dielectric constant and magnetocapacitance measurements were conducted using a custom-built probe integrated into a Quantum Design Physical Property Measurement System (PPMS) at the National High Magnetic Field Laboratory (NHMFL). Polycrystalline samples were pressed into pellets and thinned to a uniform thickness of approximately 0.4 mm to ensure consistency and optimal measurement conditions. Reliable electrical contacts were established by applying silver electrodes to the pellet surfaces using conductive silver epoxy.

Capacitance measurements were performed over a frequency range of 10 kHz–20 kHz using an AH 2700A ultra-precision capacitance bridge, enabling high-resolution dielectric and magnetocapacitance data acquisition under varying magnetic field strengths. For zero-field measurements, an in-house Agilent 4980AL LCR meter integrated into a Janis cryostat was utilized.

2.4. Neutron diffraction

Neutron powder diffraction was conducted at the High Flux Isotope Reactor (HFIR), Oak Ridge National Laboratory, using the HB2A diffractometer with a neutron wavelength of 2.41 Å. Data were collected at $T = 2$ K under applied magnetic fields of 0 and 50 kOe. Additional temperature-dependent neutron diffraction measurements were performed at the Spallation Neutron Source (SNS) on the POWGEN instrument, utilizing bank 3 with a central wavelength of 2.65 Å. The crystal and magnetic structures were refined using the Rietveld method implemented in the FullProf suite [40]. Magnetic representational analysis was carried out using the BASIREP program [41] within Bilbao Crystallographic Server [42] allowing for a comprehensive determination of the magnetic symmetry and structure. To minimize reorientation of the powder sample under an applied field, the polycrystalline sample was pelletized using a pellet press, annealed at 540 °C for 6 h, and subsequently broken into chunks before being loaded into aluminum cans. This method ensures that the orientation of large grains remains effectively random, reducing potential preferred orientation effects in strong magnetic fields.

2.5. DFT calculations

The DFT calculations applied to CTMO were carried out using the Vienna Ab-initio Simulation Package [43,44]. The non-empirical strongly constrained and normed (SCAN) meta-GGA functional [45] was used to sample the electron–electron interaction, such functional accurately predicts the structure and energies of many materials. The valence electrons and nuclei interaction is described using projector-augmented waves [46]. The electronic states' plane-wave expansion was optimized to 550 eV. We also used the Hubbard Hamiltonian as proposed by Dudarev et al. [47] to account for strong on-site Coulomb repulsion interactions in the magnetic Co species ($U_{eff} = 3.3$). The convergence threshold for the calculations was set to 10^{-8} eV, allowing precisions up to fractions of meV. To evaluate the electronic states in the Brillouin zone an equally distributed gamma-centered k-points mesh of $7 \times 7 \times 2$ was set.

Two sets of calculations, including scalar relativistic and spin–orbit interactions, were performed. We used two structures for the analysis,

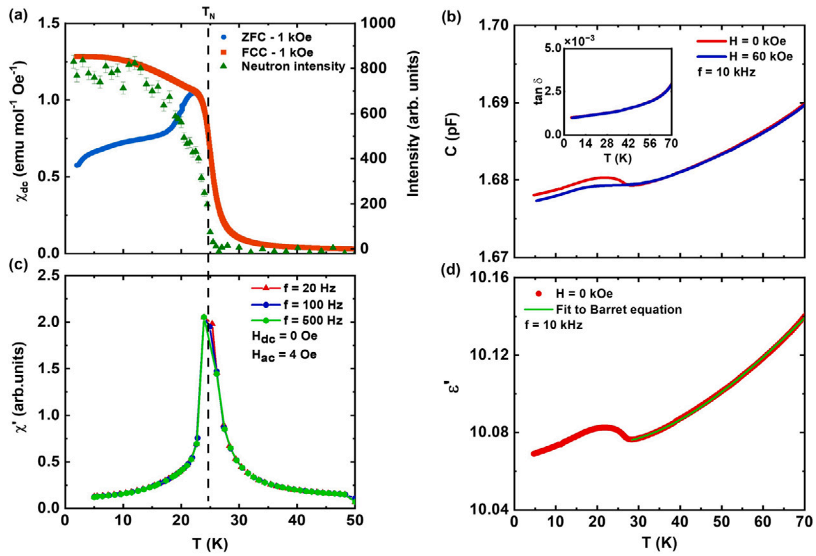

Fig. 1. Magnetic and dielectric properties of CTMO. (a) Zero-field cooled (ZFC) and field-cooled (FC) DC magnetic susceptibility (χ_{dc}) as a function of temperature (T) measured with applied magnetic field, H = 1 kOe. The green curve represents the magnetic Bragg peak intensity from neutron diffraction experiment. (b) Temperature dependence of capacitance (C) at different magnetic fields. Inset: Variation of loss tangent ($\tan\delta$) with respect to T. (c) Real part of AC magnetic susceptibility (χ') versus T at different frequencies (f). (d) Dielectric constant (ε') as a function of T, extracted from (b). The green curve in (d) represents the fit to Barrett equation. A vertical dotted line indicates the common transition temperature, T_N, determined from (a) and (c).

the experimental and one obtained after relaxing the structure using the described computational conditions. The incorporation of spin–orbit coupling allowed us to describe the Dzyaloshinskii–Moriya interaction (DMI) in CTMO, a magnetic system that lacks spatial inversion symmetry.

3. Results

3.1. Temperature dependence of magnetic properties

Fig. 1 summarizes the key experimental findings for the temperature dependence of magnetic and dielectric properties in CTMO.

The temperature dependence of zero-field-cooled (ZFC) and field-cooled (FC) DC magnetic susceptibility (χ_{dc}) measured at an applied field of 1 kOe is shown in Fig. 1(a). The bifurcation of the ZFC and FC curves around T_N = 24 K marks the onset of long-range antiferromagnetic ordering. Below 60 K, the susceptibility deviates from Curie–Weiss behavior (discussed in Appendix A). Fitting the Curie–Weiss law $\chi = C/(T-\theta)$ above 60 K yields an effective moment $\mu_{\mathrm{eff}} = 4.97\,\mu_{\mathrm{B}}$ and a Weiss temperature $\theta = -68$ K for an applied field of 20 kOe. For an applied field of 1 kOe, the fitting gives $\mu_{\mathrm{eff}} = 5.4\,\mu_{\mathrm{B}}$ and $\theta = -88$ K. These effective moment values exceed the spin-only value of $3.88\,\mu_{\mathrm{B}}$ for Co^{2+}, which might be an indication of contribution from the orbital component. The negative Weiss temperatures indicate dominant antiferromagnetic interactions, while the field-dependent effective moments suggest contributions from a temperature-independent diamagnetic background from Co core electrons and Van Vleck paramagnetism [38]. The green curve in Fig. 1(a) represents the temperature dependence of a magnetic Bragg peak intensity obtained from neutron diffraction, corroborating antiferromagnetic ordering at T_N.

Fig. 1(b) shows the temperature dependence of the capacitance at two different magnetic fields. An anomaly at T_N under zero field indicates magnetodielectric coupling. This anomaly broadens and weakens under an applied magnetic field of 60 kOe, further confirming its magnetic origin. The inset in Fig. 1(c) depicts the temperature dependence of the loss tangent ($\tan\delta$), with small values suggesting the highly insulating nature of CTMO.

Fig. 1(c) presents the real part of the AC magnetic susceptibility (χ') measured at three different frequencies. The frequency independence of the peak position in $\chi'(T)$ confirms a transition from a paramagnetic to

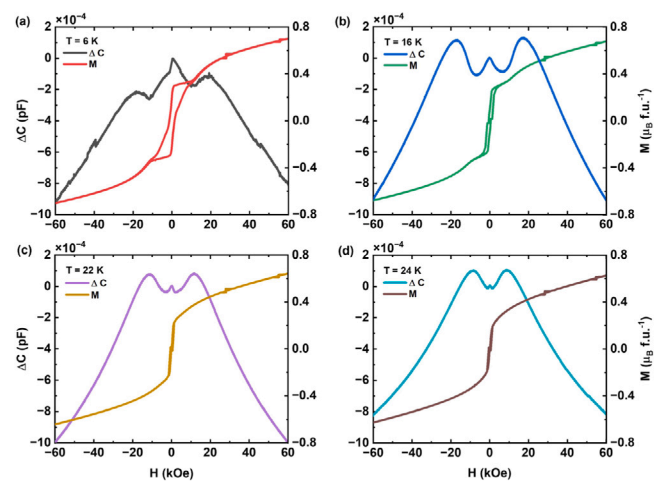

Fig. 2. Magnetic field dependence of the magnetocapacitance (ΔC=C(H)–C(0)) and magnetization (M) from H = −60 kOe to H = 60 kOe for CTMO at different temperatures. Panels (a)–(d) correspond to T = 6, 16, 22, and 24 K, respectively. The left axis represents ΔC (in pF), while M (in μ_B/f.u.) is scaled in the right y-axis.

a long-range ordered phase and rules out the presence of a spin-glass phase. Instead, the peak reflects spin or domain fluctuations near the magnetic transition.

Fig. 1(d) illustrates the temperature dependence of the relative dielectric constant (ε'), extracted from the red curve in Fig. 1(c). In general, the dielectric constant can be associated with the lattice dynamics of optical phonon modes through the Lyddane-Sachs-Teller (LST) relation:

$$\frac{\varepsilon_0}{\varepsilon_\infty} = \prod_j \frac{\omega^2_{\mathrm{LO},j}}{\omega^2_{\mathrm{TO},j}}, \tag{1}$$

where ε_0 and ε_∞ are the static and optical dielectric constants, respectively, and $\omega_{\mathrm{LO},j}$ and $\omega_{\mathrm{TO},j}$ are the longitudinal and transverse optical phonon frequencies, respectively [48,49]. In the absence of magnetodielectric coupling, the temperature dependence of ε' typically follows the modified Barrett equation [49,50]:

$$\varepsilon(T) = \varepsilon(0) + \frac{A}{\exp\left(\frac{\hbar\omega_0}{k_B T}\right) - 1}, \tag{2}$$

where A is a coupling constant, ω_0 is the mean frequency of the lowest-lying optical phonon branch, and $\varepsilon(0)$ is the static dielectric constant at zero temperature. Fitting our data above T_N yields $\varepsilon(0) = 10.07$, $A = 0.39$, and $\omega_0 = 93.4\,\mathrm{cm}^{-1}$, consistent with reported transverse optical (TO) phonon frequencies in CTMO [39,51]. Below T_N, deviations from this behavior might indicate potential spin-phonon coupling.

3.2. Field dependence of magnetization and magnetocapacitance

Fig. 2 shows the magnetic field dependence of the magnetocapacitance (ΔC) and magnetization (M) at various temperatures for CTMO. In each panel, the magnetocapacitance data (ΔC) are displayed as solid lines with distinct colors, while the corresponding magnetization data (M) are overlaid as line curves, with color-coding used to differentiate the data sets. As the magnetic field is swept from 0 kOe to ±60 kOe, two prominent features are evident in the magnetocapacitance response:

First, a pronounced dip in ΔC is observed, coinciding with the completion of the magnetization hysteresis loop. This feature reflects the alignment or reversal of magnetic domains in response to the applied magnetic field. This hysteresis could also result from magnetic anisotropies. The decrease in ΔC at this point underscores the strong coupling between the magnetic and dielectric properties in CTMO, where domain reconfigurations directly influence the dielectric constant.

Second, a distinct peak in ΔC follows the dip, corresponding to the metamagnetic transition. This transition is characterized by a rapid increase in M, indicative of a field-induced phase transition from an antiferromagnetic-like state to a more ferromagnetic state. The observed peak in ΔC reflects the dielectric response to this magnetic phase change. The position and magnitude of the peak vary with temperature, highlighting the thermal dependence of the metamagnetic transition. At higher fields, ΔC decreases, which can be attributed to the suppression of spin fluctuations as the system approaches magnetic saturation. The magnetocapacitance features are particularly pronounced at $T = 16$ K and $T = 24$ K, compared to $T = 6$ K and $T = 11$ K. At lower temperatures, reduced thermal fluctuations stabilize the magnetic phase, minimizing spin fluctuations. The presence of hysteresis in the magnetization at all temperatures reflects weak ferromagnetism due to spin canting within the system.

Fig. 3 presents the magnetic field dependence of the real part of the AC susceptibility (χ') and the magnetocapacitance (C) at two representative temperatures, $T = 11$ K and $T = 22$ K. At both temperatures, the peak in χ' coincides with a rapid change in C, signaling enhanced spin fluctuations during the metamagnetic transition. The increase in spin fluctuations at this field is reflected in the dielectric response, leading to a peak in C. At higher fields, where spin fluctuations are suppressed and the system approaches saturation, C decreases. These results highlight the critical role of spin structure and spin fluctuations in governing the magnetoelectric response in CTMO.

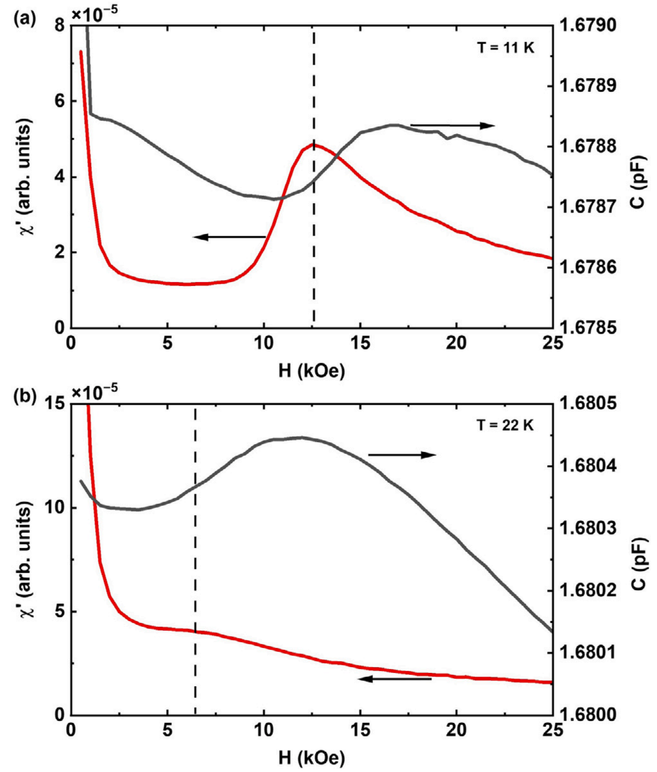

Fig. 3. Magnetic field dependence of the real part of the AC susceptibility (χ') and the magnetocapacitance (C) at (a) $T = 11$ K and (b) $T = 22$ K. The red and black lines correspond to χ' and C, respectively. The vertical dashed lines indicate the field at which a notable peak in χ' and a rapid change in C occur, highlighting the influence of spin fluctuations on the dielectric response.

3.3. Neutron diffraction

Neutron powder diffraction measurements were conducted to investigate the magnetic structures of CTMO under applied magnetic fields. Data were collected at $T = 2$ K for two field conditions: $H = 0$ kOe and $H = 50$ kOe. The diffraction patterns were refined using the FullProf Suite [40], and magnetic symmetry analysis was performed with the BASIREP program [41] within Bilbao Crystallographic Server [42]. The Rietveld refinement results and the corresponding magnetic structures are presented in Fig. 4.

The magnetic propagation vector (**k**) was determined using the k-search functionality in FullProf. At $H = 0$ kOe, the magnetic reflections were indexed with $\mathbf{k} = (0, 0, 0.5)$, indicating antiferromagnetic modulation along the c-axis. Under $H = 50$ kOe, **k** changed to $(0, 0, 0)$, corresponding to a commensurate magnetic structure with ferromagnetic alignment along the c-axis.

The parent crystal structure of CTMO belongs to the orthorhombic space group $P2_12_12$ (No. 18). For each magnetic propagation vector (**k**), there are four maximal magnetic subgroups. The first two subgroups ($Pc2_12_12_1$, BNS setting No. 19.28) allow non-zero magnetic moments within the ab-plane, while the latter two subgroups only permit magnetic moments aligned along the c-axis.

At $H = 0$ kOe with $\mathbf{k} = (0, 0, 0.5)$, the best fit was achieved with the second subgroup (BNS setting No. 19.28), yielding moment values:

$$m_a = 0.59(4)\ \mu_\mathrm{B}, \quad m_b = 3.54(3)\ \mu_\mathrm{B}, \quad m_c = 0\ \mu_\mathrm{B}. \tag{3}$$

Similarly, at $H = 50$ kOe with $\mathbf{k} = (0, 0, 0)$, the best fit was achieved with the first subgroup (BNS setting No. 19.28), yielding magnetic moments:

$$m_a = 0.88(7)\ \mu_\mathrm{B}, \quad m_b = 2.15(5)\ \mu_\mathrm{B}, \quad m_c = 0\ \mu_\mathrm{B}. \tag{4}$$

It is noteworthy that the total moment at $H = 50$ kOe is less than at $H = 0$ kOe. This discrepancy might be due to residual contributions from the antiferromagnetic phase ($\mathbf{k} = (0, 0, 0.5)$) present at $H = 0$ kOe, which was not included in the refinement. Additionally, the refinement assumes an isotropic g-factor of 2, although cobalt typically exhibits an anisotropic g-factor, which may influence the absolute moment values. Furthermore Co^{2+} systems are known to exhibit in plane magnetic anisotropies that may also influence the absolute moment estimation.

The Rietveld refinement included three phases: (1) the structural phase CTMO, (2) an aluminum structural phase due to the sample can used during the neutron diffraction experiment, and (3) the magnetic phase. Less than 3% non-magnetic impurities of unknown origin, determined to be temperature-independent, were present in the sample.

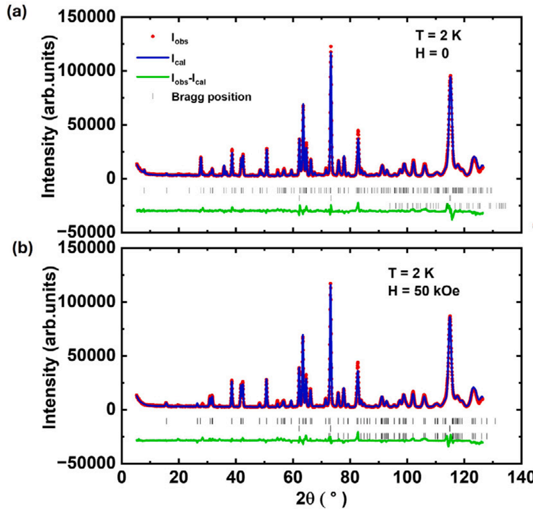

Fig. 4. Neutron diffraction spectra with Rietveld refinement at $T = 2$ K for $CoTeMoO_6$. The observed intensity (I_{obs}), the calculated intensity (I_{cal}), the difference between these two quantities ($I_{obs-I_{cal}}$), and the nuclear Bragg peak positions are represented by red dots, a solid blue line, a solid green line, and black vertical dashes, respectively. The magnetic structure is derived through representational analysis and presented to the right of each spectrum. (a) Refined spectra at $H = 0$ kOe with a determined propagation vector, $\mathbf{k} = (0, 0, 0.5)$. Agreement factors: Bragg R-factor = 8.85%, Magnetic R-factor = 15.59%, $\chi^2 = 7.87$, $R_{wp} = 12.1\%$, $R_p = 10.4\%$. (b) Refined spectra at $H = 50$ kOe with a determined propagation vector, $\mathbf{k} = (0, 0, 0)$. Agreement factors: Bragg R-factor = 10.09%, Magnetic R-factor = 20.69%, $\chi^2 = 9.4$, $R_{wp} = 14.2\%$, $R_p = 11.4\%$. (c) The magnetic structure at $H = 0$ kOe as viewed along the a-axis. (d) The magnetic structure at $H = 50$ kOe as viewed along the a-axis. (e) The magnetic structure at $H = 0$ kOe as viewed along the c-axis. (f) The magnetic structure at $H = 50$ kOe as viewed along the c-axis.

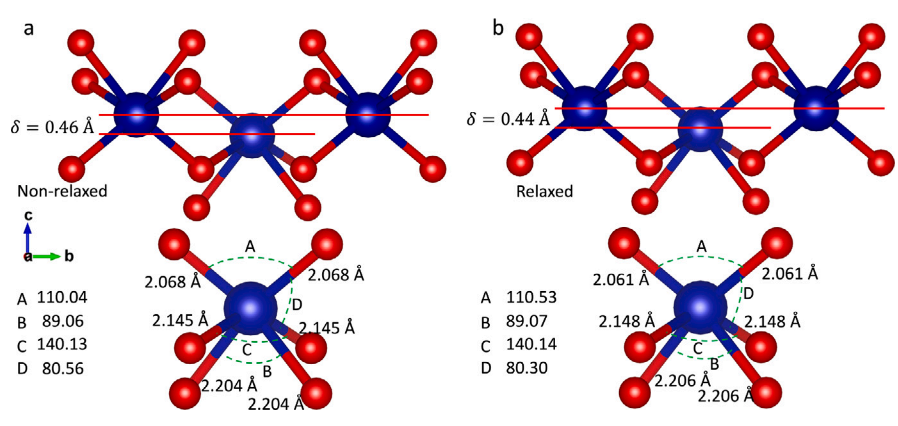

Fig. 5. Relaxed and non-relaxed structures of CTMO, illustrating CoO_6 octahedra distortions. The relaxed structure features axial Co–O bond lengths (A and D) of 2.067 Å and equatorial bond lengths (B and C) of 2.107 Å and 2.313 Å. These distortions induce anisotropic exchange interactions that stabilize the canted magnetic structure.

3.4. Comparison of magnetic structure obtained using neutron diffraction and DFT calculations

To determine the magnetic ground state of CTMO at 0 kOe, density functional theory (DFT) calculations were conducted with and without magnetic canting. These calculations assessed the energy required to induce canting and analyzed how this energy correlates with the experimental characterization temperature. Two scenarios were considered: the experimentally derived crystal structure and a fully relaxed structure without constraints. Our density functional theory (DFT) calculations indicate that the canted magnetic structure, stabilized by interlayer antiferromagnetic coupling, is strongly influenced by DM interactions and lattice local distortions. The structural distortions involve an upward displacement of the central Co atom, resulting in slight changes to bond angles and bond lengths. Co–O bond lengths exhibit anisotropy: axial bonds (A and D) extend to 2.068 Å, while equatorial bonds (B and C) remain almost without changes. This broken local symmetry introduces anisotropic exchange interactions that stabilize the observed canted magnetic structure (see Fig. 5).

Table 1 compares the structural parameters, atomic positions, and magnetic moments for the experimental data, the calculated data using the experimental lattice, and the fully relaxed structure. Upon relaxation, the CTMO structure undergoes minor contraction, particularly along the c-axis, where it decreases by approximately 0.02 Å. These small changes coincide with slight rearrangements of Co atoms in the z-direction. The a and b lattice parameters exhibit negligible variation, confirming the robustness of the computational methodology.

Neutron diffraction measurements revealed a canting angle of approximately 9.5°, which is corroborated by DFT calculations predicting 8.64° for both the self-consistent and relaxed structures. The total magnetic moment, however, is slightly overestimated, which is consistent with the limitations of plane wave basis functions.

For the non-relaxed structure, the energy required to induce canting was 1.09 meV, corresponding to a temperature of approximately 14 K. Upon structural relaxation, the needed energy increased slightly to 1.22 meV (14.64 K). These results suggest that structural distortions elevate the energy necessary for canting and stabilize the canting angle, as observed in recent studies [52]. The canting in CTMO appears to be stabilized by structural distortions around Co atoms and antisymmetric exchange interactions, such as the Dzyaloshinskii–Moriya interaction (DMI), which emerges upon incorporating spin–orbit coupling (SOC) into the calculations.

The magnetic structure at 50 kOe was also analyzed, comparing configurations with moments confined only to the ab plane and those with a c-axis component. In both cases, $\mathbf{k} = (0, 0, 0)$, indicating that the crystallographic and magnetic unit cells are identical. The solution with moments only in ab plane is energetically favored over the non coplanar solution by 0.83 meV, demonstrating that the inplane canting stabilizes ferromagnetic arrangement under magnetic fields due to intra-layer interactions. The DFT-calculated moments ($m_a = 1.000\ \mu_B$, $m_b = 2.627\ \mu_B$, $m_c = 0\ \mu_B$, resulting in $M = 2.81\ \mu_B$), with a canting angle of 20.84°, are in close agreement with the experimental values obtained from neutron diffraction ($m_a = 0.88(7)\ \mu_B$, $m_b = 2.15(5)\ \mu_B$, $m_c = 0\ \mu_B$, resulting in $M = 2.32(5)\ \mu_B$), with a canting angle of $22.2 \pm 4.5°$.

4. Discussion

The observation of a canted magnetic structure with a small canting angle ($\theta = (10 \pm 4)°$) at $H = 0$ highlights the significant role of the Dzyaloshinskii–Moriya (DM) interaction. This sizeable DM interaction originates from the chiral crystal structure and the modest spin–orbit coupling associated with Co^{2+} ions. Supporting this observation, our DFT calculations also predict a canted magnetic structure when spin–orbit coupling is included. The canting angle obtained from the experiment is slightly larger than previous experiments [37], likely due to uncertainties in the a-component of the magnetic moment and temperature-dependent effects.

Table 1
Comparison of $CoTeMoO_6$ structural parameters: Experimental vs. DFT-calculated values at $H = 0$.

Property	Experimental	Calculated	Relaxed
a (Å)	5.24	5.24	5.24
b (Å)	5.06	5.06	5.06
c (Å)	17.61	17.61	17.59
M (μ_B)	3.59 ± 0.03	2.81	2.81
Canting angle (°)	10 ± 4	8.64	8.64

Note: Experimental values are determined at 2 K. Calculated and Relaxed values are obtained from DFT simulations. The relaxed structure slightly adjusts the c parameter while preserving the experimental a and b.

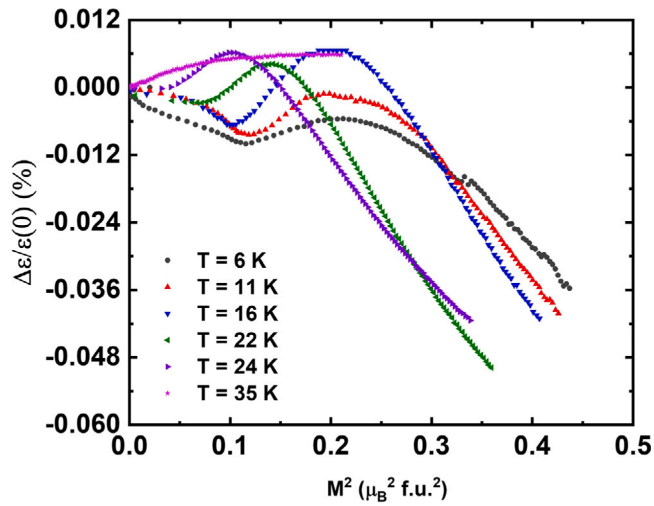

Fig. 6. Dependence of $\Delta\epsilon$ on M^2 in CTMO. While the behavior at high fields shows a linear trend, the low-field variation is dominated by spin fluctuations. Moreover, the curves at different temperatures do not collapse onto a single universal line, indicating the presence of additional contributing factors.

At $H = 50$ kOe, the canting angle increases to $\theta = (22.3 \pm 3.8)°$, reflecting field-induced spin rotation within the **ab** plane. However, the antiferromagnetic arrangement along the c-axis at zero field changes to a ferromagnetic arrangement along the c-axis in the presence of a magnetic field. In both zero field and $H = 50$ kOe, the magnetic moments remain confined within the **ab** plane, consistent with the quasi-2D nature of the system. This behavior can be attributed to the significantly larger nearest-neighbor distance along the c-axis (8.81 Å) compared to the **ab** plane (3.63 Å).

The strong correlation between the magnetocapacitance in CTMO and the magnetic ordering temperature, field-induced magnetic transitions, and spin fluctuations indicates a spin-driven magnetodielectric (MD) effect. In CTMO, a system with a canted magnetic structure, this MD effect can arise from two plausible mechanisms: (a) spin-phonon coupling mediated by magnetostriction and (b) p–d exchange interaction. These mechanisms are evaluated in detail below.

4.1. Spin–phonon coupling through magnetostriction

In the spin–phonon coupling framework, transverse optical phonon modes are renormalized as the system enters the magnetic phase or undergoes magnetic transitions induced by an external field. Variations in the dielectric constant relative to the Barrett equation (Fig. 6) and the fitted optical phonon frequency ω_0, which closely matches values reported in Raman scattering studies [39,51], along with earlier investigations [38], suggest the potential involvement of a spin-phonon coupling mechanism.

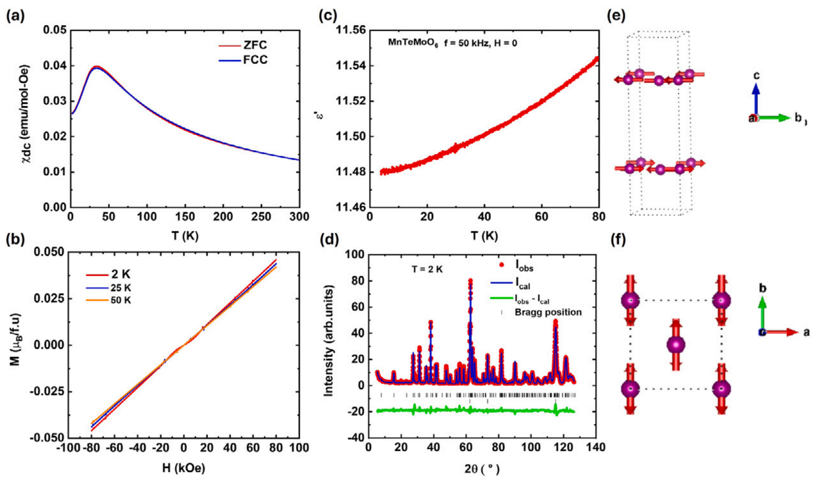

Fig. 7. (a) Temperature dependence of DC magnetic susceptibility (χ_{dc}) measured under zero-field-cooled (ZFC) and field-cooled cooling (FCC) protocols for $MnTeMoO_6$ with an applied field of 1 kOe. (b) Isothermal magnetization (M) vs. magnetic field (H) at 2 K, 25 K, and 50 K, showing linear behavior with no hysteresis. (c) Real part of the dielectric constant (ϵ') as a function of temperature at 50 kHz under zero magnetic field. (d) Rietveld refinement of neutron diffraction data for $MnTeMoO_6$ at 2 K, showing observed (I_{obs}), calculated (I_{cal}), and difference ($I_{obs} - I_{cal}$) patterns. Vertical ticks indicate Bragg reflection positions. Agreement factors: Bragg R-factor = 6.313%, Magnetic R-factor = 16.22%, χ^2 = 11.5, R_{wp} = 13.1%, R_p = 12.5%. (e) and (f) Magnetic structure of $MnTeMoO_6$ in the ab-plane and bc-plane, respectively, highlighting the collinear antiferromagnetic arrangement of Mn moments.

However, when analyzed within the Ginzburg–Landau free energy framework, where the dielectric constant variation is proportional to $\partial^2 F/\partial P^2 \sim M^2$ [13–15,22], the evidence for spin-phonon coupling becomes inconclusive. As shown in Fig. 6, the dependence of $\Delta\epsilon$ on M^2 exhibits distinct behaviors under different conditions. At low magnetic fields, the variation is dominated by spin fluctuations near the magnetic transition. Conversely, at high fields, a linear trend emerges. Despite these trends, the data across varying temperatures and fields fail to collapse onto a single universal curve, indicating that spin-phonon coupling may not be the primary driver of the observed magnetodielectric (MD) effect [13–15,22].

Furthermore, temperature-dependent neutron diffraction measurements reveal no significant anomalies in lattice parameters near T_N (Appendix C), suggesting that spin-phonon coupling is unlikely to be the dominant mechanism for the MD effect. Interestingly, crystal electric field levels calculated using the PyCrystalField software [53] reveal an energy level at approximately $\sim$13 meV, consistent with phonon frequencies observed in Raman scattering experiments. To fully elucidate the role of crystal electric field levels and phonons, further investigations involving high-resolution synchrotron X-ray diffraction, inelastic neutron scattering, and advanced crystal field calculations are essential.

4.2. *p–d* exchange interaction

The *p–d* exchange interaction originates from hybridization between Co 3*d* orbitals and O 2*p* orbitals within the CoO_6 octahedra. This hybridization modifies the superexchange pathways and induces local polarization, even without macroscopic polarization. The local polarization induced by *p–d* hybridization is proportional to:

$$P_{pd} \propto (\mathbf{S} \cdot \mathbf{e})^2 \mathbf{e},$$

where **e** is the vector from the transition metal (TM) ion to the ligand (L) [11].

In CTMO with canted magnetic structure, *p–d* hybridization produces a net dipole moment along the *c*-axis, centered on the Co^{2+} ion and its six oxygen ligands. This mechanism is supported by analogies to other chiral magnets, such as Cu_2OSeO_3 [31–33], and polar magnets like $Ba_2M_2Ge_2O_7$ (M=Co, Cu) [34–36], where *p–d* hybridization drives magnetoelectric effects. The strong correlation between the magnetocapacitance and magnetic structure in CTMO further supports this mechanism.

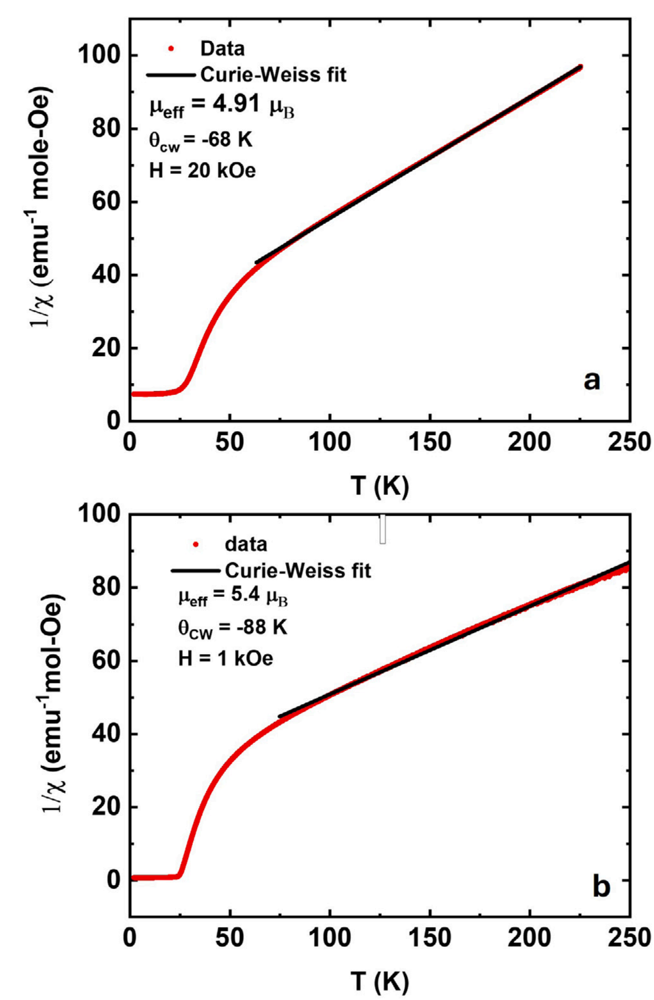

Fig. A.8. Temperature dependence of the inverse magnetic susceptibility (χ^{-1}) for CTMO measured under two applied magnetic fields: (a) 20 kOe, and (b) 1 kOe. The black lines represent fits to the Curie–Weiss law. The deviation from Curie–Weiss behavior below 60 K is attributed to quasi-two-dimensional magnetic interactions and lattice anisotropy.

Table B.2
Maximal magnetic subgroups for $P2_12_12$ (No. 18) with $k = (0, 0, 1/2)$, showing their respective settings and allowed magnetic moment components.

N	Magnetic Space Group (BNS)	Setting	Allowed magnetic moment components
1	$P_c2_12_12_1$ (#19.28)	$(a, b, 2c; 0, 0, 0)$	M_x, M_y (No M_z)
2	$P_c2_12_12_1$ (#19.28)	$(a, b, 2c; 1/4, 0, 1/2)$	M_x, M_y (No M_z)
3	$P_c2_12_12$ (#18.21)	$(a, b, 2c; 0, 0, 0)$	M_z (No M_x, M_y)
4	$P_c2_12_12$ (#18.21)	$(a, b, 2c; 0, 0, 1/2)$	M_z (No M_x, M_y)

Table B.3
Maximal magnetic subgroups for $P2_12_12$ (No. 18) with $k = (0, 0, 0)$, showing their respective settings and allowed magnetic moment components.

N	Magnetic Space Group (BNS)	Setting	Allowed magnetic moment components
1	$P2_12'_12'$ (#18.19)	Parent setting	M_x, M_y (No M_z)
2	$P2_12'_12'$ (#18.19)	Alternative domain (-b, a, c)	M_x, M_y (No M_z)
3	$P2'_12_12$ (#18.18)	Parent setting	M_z (No M_x, M_y)
4	$P2_12_12$ (#18.16)	Parent setting	M_z (No M_x, M_y)

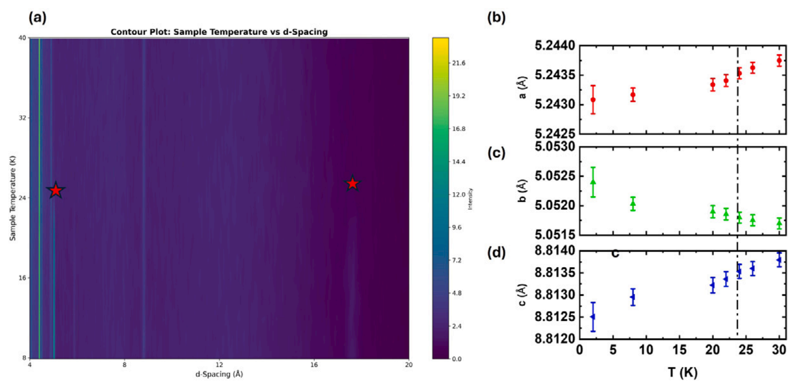

Fig. C.9. (a) Contour plot of intensity as a function of temperature and d-spacing, with brighter colors indicating higher intensity. The red stars represent the position of magnetic peaks that disappear above 24 K. (b), (c), and (d) depict the temperature-dependent lattice parameters a, b, and c, respectively. The dashed vertical line marks the magnetic ordering temperature at 24 K. Error bars represent experimental uncertainties.

4.3. Comparison with MTMO

The isostructural $MnTeMoO_6$ (MTMO) provides a useful comparison to CTMO. The results of magnetic, dielectric, and magnetic structure characterization for MTMO are presented in Fig. 7. MTMO exhibits no magnetodielectric (MD) coupling, as evidenced by its collinear antiferromagnetic order and the absence of dielectric anomalies near the magnetic transition temperature.

This lack of MD behavior might be attributed to the electronic configuration of Mn^{2+} ($3d^5$), which lacks orbital angular momentum and consequently exhibits weaker spin–orbit coupling and Dzyaloshinskii–Moriya (DM) interactions [54–57]. Furthermore, the more spherically symmetric crystal field environment of Mn^{2+} likely suppresses *p*–*d* hybridization, thereby preventing the induction of local dipole moments.

5. Conclusion

$CoTeMoO_6$ (CTMO) exhibits a quasi-2D magnetic structure with in-plane canted magnetic moments, alongside significant magnetodielectric (MD) behavior. Two plausible mechanisms drive this behavior: (a) spin–phonon coupling mediated by magnetostriction and (b) spin-dependent *p*–*d* hybridization. The resemblance of CTMO behavior to other chiral and polar magnets suggests that *p*–*d* hybridization might be the primary mechanism, while spin-phonon coupling plays a secondary role, as transition metal oxides are known to possess multiple coupling pathways. Future studies focusing on high-resolution neutron scattering, synchrotron diffraction, and advanced computational modeling are essential to disentangle these mechanisms and deepen our understanding of MD coupling in complex oxides.

CRediT authorship contribution statement

Brady Wilson: Writing – original draft, Methodology, Investigation, Formal analysis, Data curation. **Ananta Raj Acharya:** Methodology. **Eun Sang Choi:** Resources, Methodology. **Ram Rai:** Resources, Methodology. **Qiang Zhang:** Validation, Resources. **Stuart Calder:** Validation, Resources. **Rafael Gonzalez-Hernandez:** Writing – review & editing, Software, Formal analysis. **Jonathan Guerrero Sanchez:** Writing – review & editing, Software, Formal analysis. **Chetan Dhital:** Writing – review & editing, Writing – original draft, Visualization, Validation, Supervision, Software, Resources, Project administration, Methodology, Investigation, Funding acquisition, Formal analysis, Data curation, Conceptualization.

Declaration of competing interest

The authors declare that they have no known competing financial interests or personal relationships that could have appeared to influence the work reported in this paper.

Acknowledgments

This work was supported by the National Science Foundation under Grant No. NSF DMR-2213443. A portion of this research was conducted at the National High Magnetic Field Laboratory, which is supported by the National Science Foundation through Cooperative Agreement No. DMR-2128556 and the State of Florida. Neutron scattering experiments were carried out at the High Flux Isotope Reactor and Spallation Neutron Source, DOE Office of Science User Facilities operated by

Oak Ridge National Laboratory. Beam time was allocated on HB2A under proposal number IPTS-30318.1 and on POWGEN under proposal number IPTS-33738.1. We acknowledge partial financial support from DGAPA-UNAM through project IG101124. Computational work was performed at the DGCTIC-UNAM Supercomputing Center under project LANCAD-UNAM-DGTIC-368.

Appendix A. Magnetic susceptibility of CTMO

The magnetic susceptibility of CTMO deviates from Curie–Weiss behavior below 60 K, likely due to the quasi-two-dimensional nature of the magnetic interactions and anisotropy between the a- and b-axes in the orthorhombic lattice structure (see Fig. A.8).

Appendix B. Symmetry analysis of magnetic subgroups

This appendix presents the symmetry analysis for the maximal magnetic subgroups of the parent space group $P2_12_12$ (No. 18) with the propagation vectors $k = (0, 0, 1/2)$ and $k = (0, 0, 0)$. The allowed magnetic moment components for each subgroup are summarized in Tables B.2 and B.3.

Magnetic subgroups for $k = (0, 0, 1/2)$

See Table B.2.

Magnetic subgroups for $k = (0, 0, 0)$

See Table B.3.

Appendix C. Temperature-dependent lattice constants

This section presents a contour plot highlighting the temperature variation of structural and magnetic peaks, along with the temperature-dependent lattice constants of CTMO. The temperature-dependent neutron diffraction measurements were performed using the POWGEN instrument at the Spallation Neutron Source (SNS). Additionally, the lattice parameters at 2 K were obtained from the HB2A powder diffractometer (see Fig. C.9).

Data availability

Data will be made available on request.

References

[1] C. Rao, A. Sundaresan, R. Saha, Multiferroic and magnetoelectric oxides: the emerging scenario, J. Phys. Chem. Lett. 3 (16) (2012) 2237–2246.
[2] N.A. Spaldin, R. Ramesh, Advances in magnetoelectric multiferroics, Nat. Mater. 18 (3) (2019) 203–212.
[3] W. Eerenstein, N. Mathur, J.F. Scott, Multiferroic and magnetoelectric materials, Nature 442 (7104) (2006) 759–765.
[4] S. Dong, H. Xiang, E. Dagotto, Magnetoelectricity in multiferroics: a theoretical perspective, Natl. Sci. Rev. 6 (4) (2019) 629–641.
[5] C.A. Vaz, J. Hoffman, C.H. Ahn, R. Ramesh, Magnetoelectric coupling effects in multiferroic complex oxide composite structures, Adv. Mater. 22 (26–27) (2010) 2900–2918.
[6] S. Dong, J.-M. Liu, Recent progress of multiferroic perovskite manganites, Modern Phys. Lett. B 26 (09) (2012) 1230004.
[7] H.J. Molegraaf, J. Hoffman, C.A. Vaz, S. Gariglio, D. van der Marel, C.H. Ahn, J.-M. Triscone, Magnetoelectric effects in complex oxides with competing ground states, Adv. Mater. 21 (34) (2009) 3470–3474.
[8] T. Katsufuji, H. Takagi, Coupling between magnetism and dielectric properties in quantum paraelectric eutio 3, Phys. Rev. B 64 (5) (2001) 054415.
[9] V. Kocsis, Y. Tokunaga, T. Rõ om, U. Nagel, J. Fujioka, Y. Taguchi, Y. Tokura, S. Bordács, Spin-lattice and magnetoelectric couplings enhanced by orbital degrees of freedom in polar multiferroic semiconductors, Phys. Rev. Lett. 130 (2023) 036801, http://dx.doi.org/10.1103/PhysRevLett.130.036801, URL https://link.aps.org/doi/10.1103/PhysRevLett.130.036801.
[10] K. Park, J. Kim, S. Choi, S. Fan, C. Kim, D. Oh, N. Lee, S.-W. Cheong, V. Kiryukhin, Y. Choi, et al., Spin–phonon interactions and magnetoelectric coupling in co4 b 2o9 (b= nb, ta), Appl. Phys. Lett. 122 (18) (2023).
[11] Y. Tokura, S. Seki, N. Nagaosa, Multiferroics of spin origin, Rep. Progr. Phys. 77 (7) (2014) 076501.
[12] J. Kreisel, M. Kenzelmann, Multiferroics-the challenge of coupling magnetism and ferroelectricity, Europhys. News 40 (5) (2009) 17–20.
[13] G. Lawes, T. Kimura, C. Varma, M. Subramanian, N. Rogado, R. Cava, A. Ramirez, Magnetodielectric effects at magnetic ordering transitions, Prog. Solid State Chem. 37 (1) (2009) 40–54.
[14] G. Lawes, A. Ramirez, C. Varma, M. Subramanian, Magnetodielectric effects from spin fluctuations in isostructural ferromagnetic and antiferromagnetic systems, Phys. Rev. Lett. 91 (25) (2003) 257208.
[15] R. Tackett, G. Lawes, B.C. Melot, M. Grossman, E.S. Toberer, R. Seshadri, Magnetodielectric coupling in mn 3 o 4, Phys. Rev. B— Condens. Matter Mater. Phys. 76 (2) (2007) 024409.
[16] T. Suzuki, T. Katsufuji, Magnetodielectric properties of spin–orbital coupled system mn 3 o 4, Phys. Rev. B— Condens. Matter Mater. Phys. 77 (22) (2008) 220402.
[17] Y. Chang, A. Pal, P. Yen, C. Wang, S. Giri, G. Blake, J. Gainza, M.-J. Hsieh, J.-Y. Lin, C. Huang, et al., Field-induced transformation of complex spin ordering and magnetodielectric and magnetoelastic coupling in mngeteo 6, Phys. Rev. B 110 (6) (2024) 064405.
[18] M.C. Kemei, J.K. Harada, R. Seshadri, M.R. Suchomel, Structural change and phase coexistence upon magnetic ordering in the magnetodielectric spinel mn 3 o 4, Phys. Rev. B 90 (6) (2014) 064418.
[19] A. Ramirez, G. Lawes, T. Kimura, C. Varma, M. Subramanian, Progress in magnetoelectronics, in: Strongly Correlated Electron Materials: Physics and Nanoengineering, Vol. 5932, SPIE, 2005, pp. 275–282.
[20] T. Kimura, S. Kawamoto, I. Yamada, M. Azuma, M. Takano, Y. Tokura, Magnetocapacitance effect in multiferroic bimno 3, Phys. Rev. B 67 (18) (2003) 180401.
[21] R. Dubrovin, N. Siverin, M. Prosnikov, V. Chernyshev, N. Novikova, P. Christianen, A. Balbashov, R. Pisarev, Lattice dynamics and spontaneous magnetodielectric effect in ilmenite cotio3, J. Alloys Compd. 858 (2021) 157633.
[22] J.K. Harada, L. Balhorn, J. Hazi, M.C. Kemei, R. Seshadri, Magnetodielectric coupling in the ilmenites m tio 3 (m+ co, ni), Phys. Rev. B 93 (10) (2016) 104404.
[23] K. Dey, S. Sauerland, J. Werner, Y. Skourski, M. Abdel-Hafiez, R. Bag, S. Singh, R. Klingeler, Magnetic phase diagram and magnetoelastic coupling of nitio 3, Phys. Rev. B 101 (19) (2020) 195122.
[24] B. Lorenz, Y. Wang, Y. Sun, C. Chu, Large magnetodielectric effects in orthorhombic ho mn o 3 and y mn o 3, Phys. Rev. B— Condens. Matter Mater. Phys. 70 (21) (2004) 212412.
[25] R.C. Rai, J. Cao, L.I. Vergara, S. Brown, J.L. Musfeldt, D.J. Singh, G. Lawes, N. Rogado, R.J. Cava, X. Wei, High energy magnetodielectric effect in Kagome staircase materials, Phys. Rev. B 76 (17) (2007) 174414, http://dx.doi.org/10.1103/PhysRevB.76.174414.
[26] D.P. Panda, P. Yanda, S.S. Behera, A. Sundaresan, Magnetic, magnetodielectric, and magnetocaloric properties of new polar oxides rcrwo6 (r= sm, eu, gd, and tb), Solid State Commun. 353 (2022) 114843.
[27] C. Dhital, R. Dally, D. Pham, T. Keen, Q. Zhang, P. Siwakoti, R. Nepal, R. Jin, R. Rai, Magnetic structure of magnetoelectric multiferroic hofewo6, J. Magn. Magn. Mater. 544 (2022) 168725.
[28] S. Ghara, F. Fauth, E. Suard, J. Rodriquez-Carvajal, A. Sundaresan, Synthesis, structure, and physical properties of the polar magnet dycrwo6, Inorg. Chem. 57 (20) (2018) 12827–12835.
[29] S. Yang, H. Bao, D. Xue, C. Zhou, J. Gao, Y. Wang, J. Wang, X. Song, Z. Sun, X. Ren, et al., Magnetodielectric effect from the onset of ferrimagnetic transition in cocr2o4, J. Phys. D: Appl. Phys. 45 (26) (2012) 265001.
[30] S. Zhu, C. Shi, G. Zhao, W. Yang, H. Chen, X. Ma, J. Zhou, B. Kang, J.-K. Bao, S. Cao, Magnetodielectric effect and significant magnetoelectric coupling of co3ninb2o9 single crystal, Ceram. Int. 48 (17) (2022) 25064–25069.
[31] I. Apostolova, Dielectric and phonon properties of the multiferroic ferrimagnet cu2oseo3, J. Appl. Phys. 115 (6) (2014).
[32] E. Ruff, P. Lunkenheimer, A. Loidl, H. Berger, S. Krohns, Magnetoelectric effects in the skyrmion host material cu2oseo3, Sci. Rep. 5 (1) (2015) 15025.
[33] S. Seki, X. Yu, S. Ishiwata, Y. Tokura, Observation of skyrmions in a multiferroic material, Sci. 336 (6078) (2012) 198–201.
[34] J.W. Kim, S. Khim, S.H. Chun, Y. Jo, L. Balicas, H. Yi, S.-W. Cheong, N. Harrison, C. Batista, J. Hoon Han, et al., Manifestation of magnetic quantum fluctuations in the dielectric properties of a multiferroic, Nat. Commun. 5 (1) (2014) 4419.
[35] K. Yamauchi, P. Barone, S. Picozzi, Theoretical investigation of magnetoelectric effects in ba 2 coge 2 o 7, Phys. Rev. B— Condens. Matter Mater. Phys. 84 (16) (2011) 165137.
[36] H. Murakawa, Y. Onose, S. Miyahara, N. Furukawa, Y. Tokura, Comprehensive study of the ferroelectricity induced by the spin-dependent d-p hybridization mechanism in ba 2 x ge 2 o 7 (x= mn, co, and cu), Phys. Rev. B— Condens. Matter Mater. Phys. 85 (17) (2012) 174106.

[37] Y. Doi, R. Suzuki, Y. Hinatsu, K. Ohoyama, Crystal structures and magnetic properties of two-dimensional antiferromagnets co1-xznxtemoo6, J. Solid State Chem. 182 (12) (2009) 3232–3237, http://dx.doi.org/10.1016/j.jssc.2009.09.008, URL https://www.sciencedirect.com/science/article/pii/S0022459609004435.

[38] A. Pal, T.W. Kuo, C.-H. Hsu, D.C. Kakarla, A. Tiwari, M.C. Chou, A. Patra, P. Yanda, E. Blundo, A. Polimeni, A. Sundaresan, F.C. Chuang, H.D. Yang, Interplay of lattice, spin,and dipolar properties in $cotemoo_6$: Emergence of griffiths-like phase, metamagnetic transition, and magnetodielectric effect, Phys. Rev. B 105 (2022) 024420, http://dx.doi.org/10.1103/PhysRevB.105.024420, URL https://link.aps.org/doi/10.1103/PhysRevB.105.024420.

[39] K. Szymborska-Mazek, M. Maczka, T.A. da Silva, W. Paraguassu, A. Majchrowski, Lattice dynamics and high-pressure raman scattering studies of $cotemoo_6$ crystal, Vib. Spectrosc. 84 (2016) 153–158, http://dx.doi.org/10.1016/j.vibspec.2016.03.014.

[40] J. Rodriguez-Carvajal, FULLPROF: A program for rietveld refinement and pattern matching analysis, in: Laboratoire LÉon Brillouin (CEA-CNRS), France, 1993, available at: https://www.ill.eu/sites/fullprof/.

[41] J.M. Pérez-Mato, S.V. Gallego, E.S. Tasci, L. Elcoro, G. de la Flor, M.I. Aroyo, Symmetry-based computational tools for magnetic crystallography, Annu. Rev. Mater. Res. 45 (2015) 217–248, http://dx.doi.org/10.1146/annurev-matsci-070214-021008, bASIREP and Bilbao Crystallographic Server tools are discussed..

[42] M.I. Aroyo, A. Kirov, C. Capillas, J.M. Perez-Mato, H. Wondratschek, Bilbao crystallographic server. ii. representations of crystallographic point groups and space groups, Acta Crystallogr. Sect. A 67 (2011) 202–221, http://dx.doi.org/10.1107/S0108767311004942, bilbao Crystallographic Server as a comprehensive symmetry resource..

[43] G. Kresse, J. Furthmüller, Efficiency of ab-initio total energy calculations for metals and semiconductors using a plane-wave basis set, Comput. Mater. Sci. 6 (1) (1996) 15–50, http://dx.doi.org/10.1016/0927-0256(96)00008-0, URL https://www.sciencedirect.com/science/article/pii/0927025696000080.

[44] G. Kresse, J. Furthmüller, Efficient iterative schemes for ab initio total-energy calculations using a plane-wave basis set, Phys. Rev. B 54 (1996) 11169–11186, http://dx.doi.org/10.1103/PhysRevB.54.11169, URL https://link.aps.org/doi/10.1103/PhysRevB.54.11169.

[45] J. Sun, A. Ruzsinszky, J.P. Perdew, Strongly constrained and appropriately normed semilocal density functional, Phys. Rev. Lett. 115 (2015) 036402, http://dx.doi.org/10.1103/PhysRevLett.115.036402, URL https://link.aps.org/doi/10.1103/PhysRevLett.115.036402.

[46] D. Hobbs, G. Kresse, J. Hafner, Fully unconstrained noncollinear magnetism within the projector augmented-wave method, Phys. Rev. B 62 (2000) 11556–11570, http://dx.doi.org/10.1103/PhysRevB.62.11556, URL https://link.aps.org/doi/10.1103/PhysRevB.62.11556.

[47] S.L. Dudarev, G.A. Botton, S.Y. Savrasov, C.J. Humphreys, A.P. Sutton, Electron-energy-loss spectra and the structural stability of nickel oxide: An lsda+u study, Phys. Rev. B 57 (1998) 1505–1509, http://dx.doi.org/10.1103/PhysRevB.57.1505, URL https://link.aps.org/doi/10.1103/PhysRevB.57.1505.

[48] K. Wakamura, T. Arai, Effect of magnetic ordering on phonon parameters for infrared active modes in ferromagnetic spinel $cdcr_2s_4$, J. Appl. Phys. 63 (1988) 5824–5826, http://dx.doi.org/10.1063/1.340368.

[49] U. Adem, L. Wang, D. Fausti, W. Schottenhamel, P.H.M. van Loosdrecht, A. Vasiliev, L.N. Bezmaternykh, B. Büchner, C. Hess, R. Klingeler, Magnetodielectric and magnetoelastic coupling in $tbfe_3(bo_3)_4$, Phys. Rev. B 82 (2010) 064406, http://dx.doi.org/10.1103/PhysRevB.82.064406.

[50] P.T. Barton, M.C. Kemei, M.W. Gaultois, S.L. Moffitt, L.E. Darago, R. Seshadri, M.R. Suchomel, B.C. Melot, Structural distortion below the néel temperature in spinel $geco_2o_4$, Phys. Rev. B 90 (2014) 064105, http://dx.doi.org/10.1103/PhysRevB.90.064105.

[51] M. Mączka, K. Hermanowicz, A. Majchrowski, Łukasz Kroenke, A. Pietraszko, M. Ptak, Growth and characterization of nonlinear optical telluromolybdate cotemoo6 single crystals, J. Solid State Chem. 220 (2014) 142–148, http://dx.doi.org/10.1016/j.jssc.2014.08.023, URL https://www.sciencedirect.com/science/article/pii/S0022459614003788.

[52] Y. Li, J. Coles, X. Gui, H. Park, Y. Wu, X. Chen, J. han Chen, X. Wang, H. Cao, S. Stadler, O. Chmaissem, D.P. Young, S. Rosenkranz, J.F. DiTusa, Structural and magnetic properties of $cotemoo_6$ revisited, 2024, arXiv:2412.11233 URL https://arxiv.org/abs/2412.11233.

[53] A. Scheie, Pycrystalfield: software for calculation, analysis and fitting of crystal electric field hamiltonians, J. Appl. Crystallogr. 54 (1) (2021) 356–362.

[54] J. Kanamori, Superexchange interaction and symmetry properties of electron orbitals, J. Phys. Chem. Solids 10 (2) (1959) 87–98, http://dx.doi.org/10.1016/0022-3697(59)90061-7, URL https://www.sciencedirect.com/science/article/pii/0022369759900617.

[55] D.I. Khomskii, Transition Metal Compounds, Cambridge University Press, Cambridge, UK, 2014, http://dx.doi.org/10.1017/CBO9781139096780.

[56] J.B. Goodenough, Magnetism and the Chemical Bond, Wiley-Interscience, New York, NY, USA, 1963.

[57] C.J. Ballhausen, Introduction To Ligand Field Theory, McGraw-Hill, New York, NY, USA, 1962.